Extension of Methane Emission Rate Distribution for Permian Basin Oil and Gas Production Infrastructure by Aerial LiDAR

William M. Kunkel,* Asa E. Carre-Burritt, Grant S. Aivazian, Nicholas C. Snow, Jacob T. Harris, Tagert S. Mueller, Peter A. Roos, and Michael J. Thorpe*

Bridger Photonics, Inc., 2310 University Way Bldg 4-4, Bozeman, MT 59715, USA

E-mail: William.Kunkel@bridgerphotonics.com; Mike.Thorpe@bridgerphotonics.com

Abstract

Aerial LiDAR measurements at 7474 oil and gas production facilities in the Permian Basin yield a measured methane emission rate distribution extending to the detection sensitivity of the method, 2 kg/h at 90% probability of detection. Emissions are found at 38.3% of facilities scanned, a significantly higher proportion than reported in lower-sensitivity campaigns. LiDAR measurements are analyzed in combination with measurements of the heavy tail portion of the distribution ($>$ 600 kg/h) obtained from an airborne solar infrared imaging spectrometry campaign by Carbon Mapper (CM). A joint distribution is found by fitting the aligned LiDAR and CM data. By comparing the aerial samples to the joint distribution, the practical detection sensitivity of the CM 2019 campaign is found to be 280 kg/h [256, 309] (95% confidence) at 50% probability of detection for facility-sized emission sources. With respect to the joint model distribution and its confidence interval, the LiDAR campaign is found to have measured 103.6% [93.5%, 114.2%] of the total emission rate predicted by the model for equipment-sized emission sources ($\sim$ 2 m diameter) with emission rates above 3 kg/h,

whereas the CM 2019 campaign is found to have measured 39.7% [34.6%, 45.1%] of the same quantity for facility-sized sources (150 m diameter) above 10 kg/h. The analysis is repeated with data from CM 2020-21 campaigns with similar results. The combined distributions represent a more comprehensive view of the emission rate distribution in the survey area, revealing the significance of previously underreported emission sources at rates below the detection sensitivity of some emissions monitoring campaigns.

Introduction

Methane is a potent greenhouse gas with a warming potential 80 times greater than that of CO_2 in a 20-year time frame.[1] Its current global emission rate is great enough to impact the climate significantly, with a greater contribution to global temperature rise in the first ten years after emission than CO_2 at current emission rates of both gases.[2] Consequently, mitigation of methane emissions is viewed as particularly important for meeting climate goals within the next decade. Economic sectors including agriculture, waste disposal, and energy are recognized as leading contributors to anthropogenic methane emissions, representing domains where emissions can be most meaningfully mitigated. In the oil and natural gas (O&G) industry, emissions arise from discrete infrastructure elements and associated processes that can often be addressed with targeted intervention. Mitigation involves both the detection of emission sources and follow-up with repair and/or upgrade of emitting equipment. Identifying the most important emissions drivers and tracking the efficacy of mitigation efforts is key to making emissions reductions effective and efficient.[3,4]

Broadening the view of emissions from individual sources to a distribution of sources provides large-scale context to set meaningful mitigation goals. Past characterization of methane emission distributions has often relied on bottom-up estimates based on emission factors, such as those used for the U.S. Environmental Protection Agency's Greenhouse Gas Reporting Program and Greenhouse Gas Inventory. These estimates aim to identify dominant emission sources at the component or equipment levels but have been shown to misrepresent large-scale methane emissions distributions and the relative contribution of different elements,[3,5–8] with the greatest discrepancies existing in the production sector.[9] In addition, emissions factors are meant to apply nationally, whereas emission intensities in fact vary regionally and mitigation is performed locally.[7,8] To more precisely account for emissions and to inform mitigation efforts, measurement campaigns have been conducted to obtain locally relevant empirical data within individual production basins throughout the United States and Canada.[10–15]

Many recent research efforts have focused on the Permian Basin because of its sizable share of U.S. O&G production, comprising 43% of domestic oil and 22% of natural gas produced annually.[16] Two studies on 2018/2019 Permian methane emissions both estimated region-wide O&G methane intensity to be 3.7% of production,[17,18] exceeding an estimated national average of 2.3% for the full supply chain.[7] More recent work provided methane intensity estimates in the range of 5-6% in 2018, decreasing to 3-4% in 2020.[19] Aerial measurements conducted in 2019-21 coupled with simulated emission sources representing the unmeasured part of the distribution provided a Permian Basin methane intensity estimate of 5.29%.[20] With the exception of Ref. 20, these studies leveraged satellite observations for inversion modeling and mass balance calculations, which are useful in benchmarking overall emissions but lack the detection sensitivity or spatial resolution needed to identify individual methane sources and understand their relation to infrastructure elements.

To provide a more specific account of emission sources, aerial campaigns conducted by Carbon Mapper (CM) and a separate one reported by Chen et al. performed emissions measurements in the Permian Basin using solar infrared imaging spectrometers. The first CM campaign[21] took place in 2019 and covered 55,000 km^2 in the Midland and Delaware sub-basins located in Texas and New Mexico. Emission sources were localized and attributed to individual facilities. Repeated sampling of the same sources was used to evaluate emission intermittency. Highly intermittent sources (0-25% observed persistence of facility-sized sources) were responsible for 48% of all point source emissions in the sample. Further campaigns were run in the Permian Basin in 2020-21[22] in a spatial domain partially overlapping with the 2019 campaign, with otherwise similar collection parameters.

The study by Chen et al.[23] was focused on the New Mexico Permian and encompassed over 90% of wellheads in that region. Chen et al. compared the measured emission rate distribution from their study to CM 2019 in an overlapping spatial region and found that the CM 2019 campaign detected progressively fewer emission sources at rates below roughly 300 kg/h, while their own study observed similarly reduced detections below 100-150 kg/h. Though the decline in detected emission sources suggests that the CM 2019 data under-represent the actual emission sources present below the detection sensitivity, the heavy tail portion of the data set can still valuably inform models of the emission rate distribution.

For the present work, CM data are combined and compared to compiled survey data from Bridger Photonics' first generation Gas Mapping LiDAR (GML) sensor. Emission rates in the range of 3-300 kg/h, which are underrepresented in the CM campaigns, are detected by GML at their true frequency. In a complementary manner, the CM campaign data sets offer extensive sampling of large-rate but infrequently-emitting sources. Detection data from CM and GML campaigns are joined to obtain a comprehensive view of the emission rate distribution in the survey region. Emission sources at rates observable by GML but not by CM are seen to contribute most of the total rate for the whole distribution.

Methods

The Bridger Photonics Gas Mapping LiDAR™ (GML) instrument is an aircraft-mounted remote sensing device that maps methane concentration with coaligned dual LiDAR measurements, geospatial data through a Global Navigation Satellite System, and aerial photography to show plume shape, identify the source of the emission, and quantify the emission rate. Coaligned range-finding and gas absorption lasers are spatially scanned in a conical pattern below the aircraft. Return signal originating from ground-based backscatter is detected at the sensor. Path-integrated gas concentration is measured using wavelength modulation spectroscopy on the 1651 nm absorption line of methane. Flux rates are found from total methane concentration integrated along the direction perpendicular to the gas flow direction, multiplied by wind speed at the measured plume height. Details of the collection platform have been described previously.[24]

For the surveys used in this paper, the GML instrument was flown at an altitude of 206 m above ground level (AGL), with a measured detection sensitivity of 0.41 kg/h per m/s wind speed at 90% probability of detection,[25] or nominally 2 kg/h at the average wind speed of 4.9 m/s in Midland, TX.[26] Scan parameters are chosen so the distance between LiDAR measurement points on the ground is at maximum 1 m.

The CM campaigns in this paper utilize two similar instruments called GAO and AVIRIS-NG based on solar infrared spectroscopic imaging. The CM data offer extensive sampling of the heavy tail of the distribution, but lower detection sensitivity and reduced spatial source resolution compared to GML. The instruments were flown at altitudes of 4.5 km and 8 km[21] AGL. High flight altitudes like these offer greater coverage rates (land area per time) but lower detection sensitivity. Performance of the CM instrument as a function of altitude has been characterized in controlled releases[27] and modeled with a robust Bayesian approach.[28] In this paper, campaign flights are grouped together regardless of altitude to assess campaign-specific performance rather than instrument performance in general. The campaign sensitivity is thus an average of the measurement sensitivity at the various conditions observed in the campaign, including flight altitude.

Whereas the spatial pixel size increases with altitude (CM: 3-8 m for 3-8 km flight altitude[29,30]), it is important to distinguish between pixel size and source resolution, or spatial area over which detected emissions are considered to come from the same source. An emission "source" in this paper means a set of synchronously or asynchronously detected plumes falling into a defined aggregation area, whereas "emitter" means a source smaller than the source resolution of the measurement system, inclusive of processing. In addition to limits imposed by image resolution, CM employs a 150 m diameter aggregation area to define its sources at roughly the size of a typical well pad.

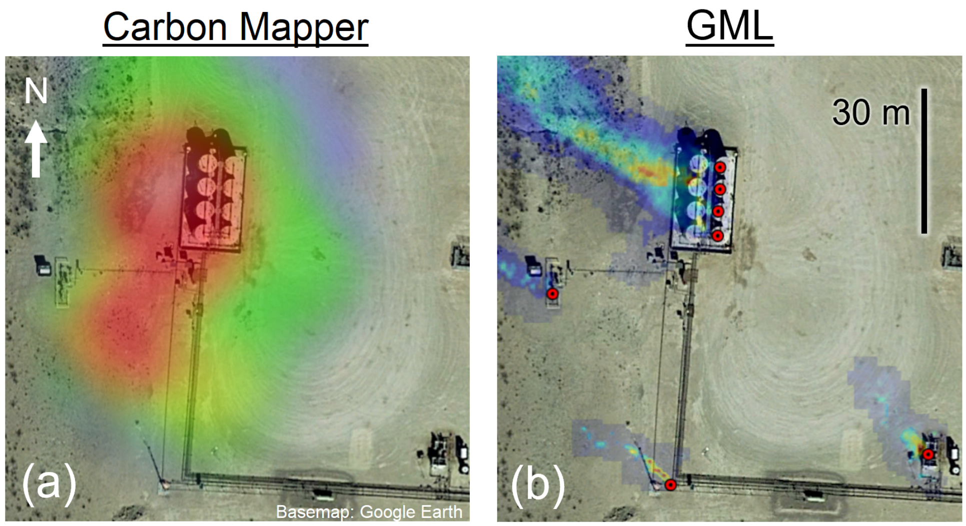

Figure 1: Example facility overlay with methane plume images from (a) CM 2019[31] and (b) GML scans superimposed on satellite imagery. GML emission locations are marked by red dots. CM 2019 and GML plumes were observed on different dates; the GML image comprises plumes observed on multiple dates. GML identifies unique emission sources at an interval of 4-5 m on a tank battery (upper center).

To compare spatial characteristics of GML and CM emission sources, consider the example plume imagery overlaid on satellite visible imagery shown in Fig. 1. The same facility was observed by both AVIRIS-NG and GML on different dates. In (a), two possible gas concentration peaks are not quite distinguishable, whereas in (b), multiple GML plumes are visible. GML pins mark localization of point sources with a precision of 2 m, which roughly corresponds to the size of typical production equipment. Asynchronous detections at these locations must be localized to within 2 m to count toward the same emission source. For CM, by contrast, all emitters within 150 m are aggregated to the same source. This tends to increase source emission rates because multiple emitters are summed to obtain the reported source rate. For comparison on an equal basis with CM, GML detections can also be aggregated to 150 m diameter groups. Cases where spatial aggregation is performed are labeled in the analysis. Further details of GML spatial aggregation are given in Sect. S1.

Further parameters, including data selection, measurement time frame, survey area, and scan repetitions were considered in compiling the data sets. Details of the data compilation are given in Sect. S2. Statistical tests on the heavy tail part of the distribution are run to check the assumption that GML and CM data sets sample the same distribution (Sect. S3).

Results

After alignment, we combine the CM and GML data sets to obtain a joint model of the emission rate distribution. We describe results in terms of the detection density and cumulative emission rate distribution. The detection sensitivity of the CM campaign is quantified by comparing the CM detection density to the joint model function, and the share of the cumulative emission rate measured by each campaign (scaled by sample size) is also inferred by comparing to the model. We first run the analysis on facility-sized sources (150 m diameter) and then repeat the process on single-emitter sources. This highlights differences between the distributions due to spatial aggregation to facility-sized sources. Results from the CM 2020-21 campaigns are also shown.

Facility-sized aggregated (150 m) emission sources

As a first step to joint analysis, we establish a comparison domain supported by both the GML and CM samples. Sensitivity limits associated with each sample determine that emission sources below the full detection limit (FDL) will be detected with diminishing probability as the emission rate decreases. The probability of detection (POD) for a given source can be characterized rigorously as a function of emission rate, wind speed, and flight altitude using controlled release data in a robust Bayesian formalism.[28] In this work we take a simple approach to restrict the emission rate domain to rates above the greater FDL of both samples. For the GML and CM samples, the limiting FDL is set by CM. We choose $x_L = 600$ kg/h as the effective FDL of the CM measurements. Accuracy of the declared FDL is not critical as long as it is large enough to avoid introducing observations at significantly reduced POD.

All distributions are presented in the single-scan equivalent form described in Sect. S2.4.1, which can be understood as a distribution on a characteristic emission rate from a single observation of a given source, subject to detection sensitivity limits of the measurement campaign. The characteristic emission rate approximates an instantaneous source emission rate that would be observed in a single overflight; spatial aggregation and multiple overflights effectively sum and average the rate across observations of the source.

Before fitting the data to obtain a joint distribution, we run a preliminary check on the sample distributions using a hypothesis test based on the Kolmogorov-Smirnov (K-S) statistic. The test is meant to show whether the GML and CM samples differ significantly above the CM FDL, that is, in the heavy tail portion of the distribution. The outcome of the test does not oppose the assumption that GML and CM samples follow the same distribution (Sect. S3).

We next create a model of the distribution that represents both samples. The model density function is taken to follow a generalized lognormal distribution,

$$p(x) \propto \exp\left(-\left|\frac{x - x_0}{b}\right|^m\right), \tag{1}$$

where x is the base-10 logarithm of the emission rate and x_0, b, and m are fit parameters where $b > 0$ and $m > 0$. Integration over the range $x_L \leq x < \infty$ yields the survival function

$$S(x) = \frac{1 - \mathrm{sgn}(x - x_0)\Gamma\left[(|x - x_0|/b)^m, \frac{1}{m}\right]}{1 - \mathrm{sgn}(x_L - x_0)\Gamma\left[(|x_L - x_0|/b)^m, \frac{1}{m}\right]}, \tag{2}$$

which has been adapted to the integration range and direction so that $\lim_{x\to\infty} S(x) = 0$ and $S(x_L) = 1$. In the special case where $m = 2$, the generalized lognormal distribution is simply lognormal. In either case, the fit parameters are jointly optimized using maximum likelihood estimation (MLE). With the joint likelihood function given in Sect. S4, the samples can be fit jointly below their respective FDLs. A nominal value of $x_L = 3$ kg/h is chosen for the GML FDL for equipment-sized sources, consistent with the sensitivity of 2 kg/h

(90% POD) mentioned in the Methods section. For facility-sized sources, this is increased to $x_L = 10$ kg/h to avoid underestimating the FDL, since spatial aggregation increases source emission rates. The MLE fitting process accounts for differences in sample size so the source densities are compared without requiring normalization based on survey size or number of overflights.

Several candidate fits are considered. The joint fit is compared to single-sample fits using lognormal and generalized lognormal forms for the density function. The purpose is to confirm that the joint fit better represents the two samples and to choose a model function that more accurately represents the two samples, particularly with respect to the "tailedness" of the distribution determined by m in Eq. 1. After obtaining fit parameters, the candidate models are assessed for relative likelihood of information loss using the Akaike information criterion (AIC).[32] The AIC comparison shows that the joint lognormal fit is optimal for 150 m emission sources (GML with CM 2019 or CM 2020-21), whereas a generalized lognormal model is preferred for equipment-sized emitters (GML with CM 2019; $m = 1.619$). Details of the AIC analysis are given in Sect. S5. Best fit parameters for all candidate models are shown in Table S1. Those from the optimal candidate provide the current best known representation of the distribution based on the GML and CM data.

With fit parameters obtained from the joint likelihood analysis, the resulting density function is shown in Fig. 2. Survey detections are binned by emission rate and the entire sample is scaled to a reference total of 1000 detected sources above the CM FDL. Error bars are placed at $\pm 2p_{\text{bin}}/\sqrt{n_{\text{bin}}}$, where p_{bin} is the density value of the bin and n_{bin} is the count of emission sources in the bin. Confidence bounds for the model fit are calculated using the likelihood ratio (LR) method at 5% rejection. The bounds consist of the most extreme value of the distribution function at every emission rate among the locus of solutions on the rejection contour. Fit agreement and scale factors are described in Sect. S6.

Though the three traces in Fig. 2 (CM 2019, GML, and model) agree above the CM FDL, CM detection density diminishes rapidly at emission rates below the full detection limit. By

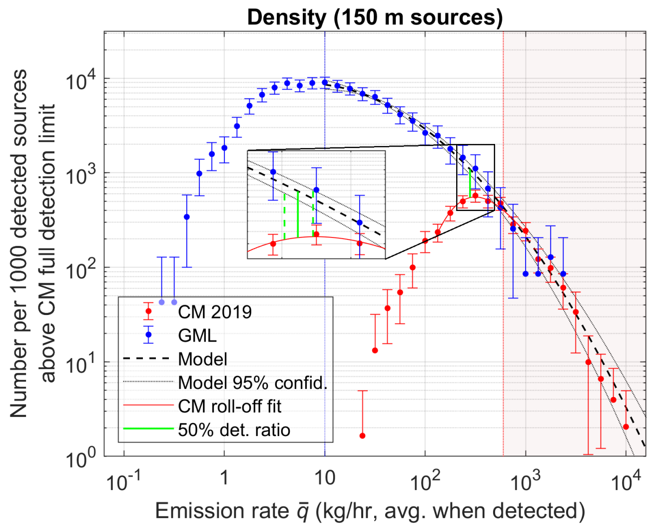

Figure 2: CM 2019 and GML emission source density as a function of emission rate, where sources have a 150 m diameter aggregation area. Zoomed in view near the sensitivity limit (inset) shows the 50% detection ratio with respect to model function and its confidence bounds. Model function follows Eq. 1 with $m = 2$, $x_0 = 0.797$, $b = 1.140$.

comparing the model to the CM detection distribution around the roll-off region using an error-weighted cubic polynomial fit of the binned data, the 50% detection ratio is placed at 280 [256, 309] kg/h, where the confidence interval (CI) is found by comparing to the 95% CI of the model fit, neglecting error in the cubic polynomial estimating the roll-off, as shown in the inset. This resulting sensitivity is considerably higher than the detection limit quoted by Cusworth et al. at 10-20 kg/h but is consistent with a previous estimate of the sensitivity in the range 100-300 kg/h.[23] Without compensation, reduced POD leads to a significant underrepresentation of emission sources below the sensitivity. For example, comparing the detection density of CM to GML binned data at 100 kg/h shows that emission sources at this rate are in fact 14 times more common than the CM data would suggest. The CM campaign can be expected to underestimate both the fraction of facilities with emissions and the total emission rate for the facilities surveyed because of its sensitivity limit. In fact, the CM 2019 campaign detected emissions at 1.48% of well sites whereas the GML detected emissions at 38.3% of facilities (see Sect. S1).

Controlled release measurements could confirm the sensitivity findings reported in this work. Alignment of flight altitude and on-the-ground properties of the sources observed in the campaign, such as ground cover, would need to be considered. Moreover, the effects of spatial aggregation would need to be accounted for to achieve the same measure of "realized" detection sensitivity for the source definition used in the campaign.

Equipment-sized emission sources

Although the above results for 150 m sources show that emission rates less than ~ 300 kg/h are underrepresented in the CM detection density, a further increase in density of lower emission rates occurs when sources are resolved to equipment size scale (~ 2 m). Facility-aggregated emission rates tend to be higher than equipment rates because co-located emitters on a site count toward the same emission source. Equipment-sized source resolution tends to be more practical for both bottom-up emissions modeling and identification for leak detection and repair.

To obtain the equipment-scale emission distribution, GML detections are considered in their native resolution (~ 2 m) and not aggregated to 150 m. Since CM sources are not reported at finer resolution, we instead manually filter them based on associated plume imagery[31] to include only sources with a single point emission (see details in Sect. S7).

The detection density for equipment-sized sources is shown in Fig. 3 with facility (150 m) detection density traces from Fig. 2 reproduced for comparison. At mid-range emission rates ($\sim$ 3-300 kg/h), density is significantly higher for equipment-sized sources than for facility-sized sources. For example, comparing the two GML traces at 10 kg/h shows that equipment sources at this emission rate are observed eight times more frequently than 150 m ones. Single-emitter filters applied to the CM data set do not appear to distort the distribution appreciably above the CM FDL. For other CM distributions (CM 2019 single emitters, CM 2020-21 150 m sources) CM detection sensitivity is assessed in a similar manner (Sect. S8).

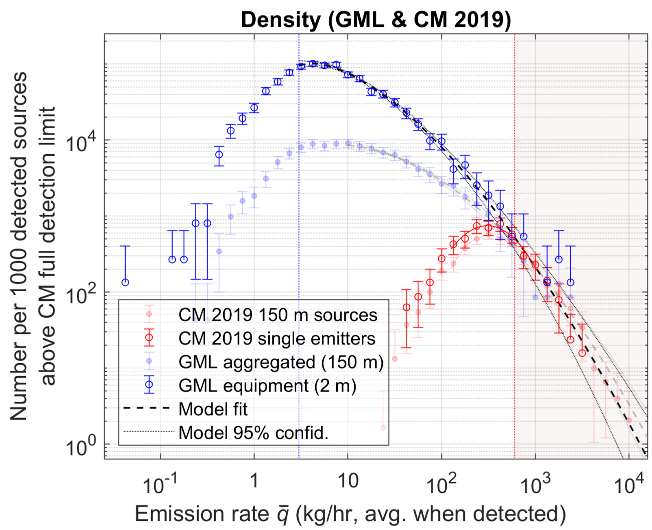

Figure 3: Density of detected emission sources with both 150 m aggregation diameter and no aggregation (single emitters), plotted together on the same axes. Model function for single emitter distribution follows Eq. 1 with $m = 1.619$, $x_0 = 0.629$, $b = 0.770$.

Cumulative emission rate distribution

The density function weighted by emission rate can be integrated to yield the cumulative emission rate distributions shown in Fig. 4. For measured samples, the cumulative sum is given by Eq. S2 (single-scan equivalent). Results for CM 2019 (150 m sources and single emitter sources) are shown in this section; cumulative emission rates for CM 2020-21 are shown in Sect. S9.

Expected error due to sample variation is shown in the plot. Error bounds show the 2.5 and 97.5 percentiles of the sample variation for an equivalently sized data set with the same number of detections above the corresponding FDL, assuming the best-fit model represents the "true" distribution. They are found by running a Monte Carlo simulation of random sets of detections drawn from the model density function (see Sect. S10). Sample error from sources with emission rates below each FDL is neglected, as is instrument quantification error. Sample variation in the heavy tail is responsible for much of the sample error along the entire trace. The relatively infrequent emitters in this emission rate range have a disproportionately large impact on cumulative emissions.

The fractional total emission rate measured in each survey can be found by comparing

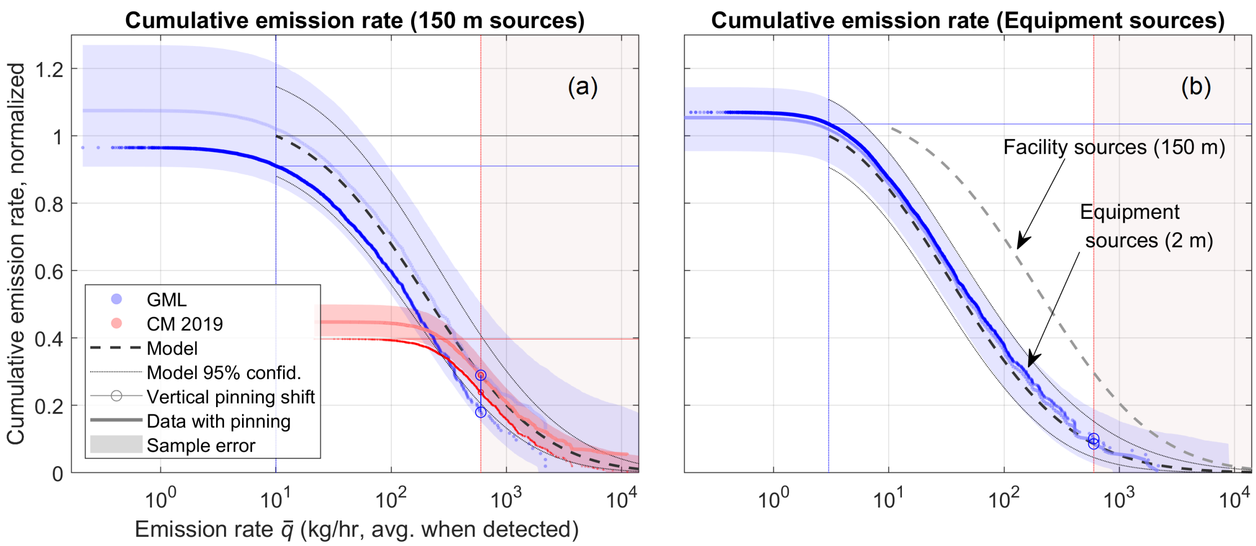

Figure 4: Cumulative emission rate distribution of (a) 150 m aggregated emission sources (GML and CM 2019) and (b) equipment sources (GML only). Error bounds (shaded regions) describe predicted sample variation. Model distribution from (a) is a reproduced in (b) for comparison. All traces are normalized to equivalent campaign scale (spatial area, number of overflights). In (b), the "facility sources" model function is multiplied by the ratio of the quantity $c(10 \text{ kg/h})/c(0)$ for each sample (see Eq. S2, single-scan equivalent) so that cumulative emissions are comparable between traces. Vertically shifted copies of survey data pinned to the value of the model distribution at the CM FDL guide the eye to suggest the shape of the measured distribution supposing sample error above the CM FDL were suppressed.

the cumulative emission rate of each sample to the model function. Since the model does not extend below the GML FDL due to the onset of sub-unity POD, we read cumulative rates at this threshold (10 kg/h for 150 m sources, 3 kg/h for equipment sources) rather than at the top of the curves. Comparing each sample to the model and its 95% CI, GML is estimated to have measured 91.1% [79.4%, 103.4%] of the total emission rate predicted by the model for 150 m sources above 10 kg/h and CM is estimated to have measured 39.7% [34.6%, 45.1%]. For equipment-scale sources, GML measured 103.6% [93.5%, 114.2%] of the cumulative emission rate above 3 kg/h. Measured fractions in excess of 100% signify the measured distribution exceeding the joint model distribution over a portion of the model CI, which can be expected from finite sample size and model fit uncertainty.

In the case of 150 m sources, both CM 2019 and GML appear to have undermeasured the heavy tail compared to the model distribution. This can be seen from the cumulative emission rates falling below the model in Fig. 4a. In fact, the measured distribution lies outside the estimated sample error, which could be explained by a departure from lognormal behavior above source emission rates of $10^{3.4}$ kg/h (see Sect. S6). The lower than expected cumulative emission rate is consistent with a sharp drop in the measured CM 2019 survival function at $10^{3.5}$ kg/h as shown in the inset of Fig. S8. By comparing the CM measured distribution to the model function in Fig. 4a, it can be seen that most of the CM-model error is indeed inherited from emission sources above $10^{3.5}$ kg/h. This suggests that either the lognormal distribution does not describe the true emission rate distribution above $10^{3.5}$ kg/h despite working well below it, or that the anomaly in CM 2019 data at $10^{3.5}$ kg/h might be explained by undersampling, systematic error, or failure of invariance assumptions mentioned in Sect. S2. In any case, further measurements of the distribution would more clearly resolve this part of the heavy tail and explain the discrepancy.

Without POD compensation, missed emissions below the detection sensitivity of a given campaign raise the apparent threshold responsible for a given share of the total emission rate. For example, according to CM 2019 data alone, 90% of the total emission rate is contributed by facilities with rates above 249 kg/h, whereas in the GML distribution the 90% facility rate is 16.9 kg/h. In fact, the true 90% threshold will be even lower because emission sources below GML detection sensitivity are underrepresented in the GML data set.

In addition, spatial aggregation of emission sources shifts (and reshapes) the entire curve to larger emission rates. Comparing the model curves in Fig. 4b shows that the 150 m source curve is shifted to the right of the equipment-level source curve by roughly a factor of 3-5 over most of the domain. The 90% threshold for the total detected emission rate shifts from 16.9 kg/h to 6.0 kg/h on the GML data traces. The shift toward smaller emission rates can be significant, meaning that measured distributions and sensitivity thresholds should be interpreted at the specified spatial aggregation level, and not directly compared at different spatial aggregation levels.

Comparing the CM and GML distributions shows that the total methane emission rate from O&G production infrastructure in the survey region is significantly greater than previously reported, with GML measuring 2.3 times that measured in the CM 2019 campaigns (and also 2.3 times that in the CM 2020-21 campaigns; see Sect. S9). If observation of emissions is viewed as an ergodic process, then the cumulative emission rate distributions shown in Figs. 4 and S11 may be seen as representative of total average emission rate for production infrastructure in the survey region. In this case, proportions of the total emission rate from the plots can be compared to measurements of regional methane flux. Based on top-down inversion from Tropospheric Monitoring Instrument (TROPOMI) measurements of regional methane flux, Cusworth et al. estimated that sources measured in the CM 2019 survey represent 59% (CM 2020-21: 49%, where fractions for each of the three campaigns are weighted by survey area) of the total methane emission rate in the survey region.[22] This estimate is somewhat higher than the proportion of cumulative emission rate measured by CM 2019 compared to GML ($1/2.3 = 43\%$), suggesting that the emission rate inferred from TROPOMI in Ref. 22 underestimates total emissions by 37% (i.e. $59\%/43\% - 1$) if GML and CM campaign data are representative of the same emissions process.

In summary, GML detection data extends the measured emission rate distribution for Permian Basin O&G production infrastructure beyond CM sensitivity limits by roughly two orders of magnitude. In joint analysis, intensive sampling of the heavy tail by CM is complemented by GML's higher detection sensitivity. In the region surveyed, facility-sized emission sources with rates below the CM campaign detection sensitivity (280 kg/h at 50% POD) contribute 67% of the total emission rate from sources with rates above 10 kg/h. The density of these sources and their constituent equipment-size emission sources (at rates above 3 kg/h), was measured without POD degradation by GML. According to the GML sample without POD correction, 90% of the total cumulative emission rate measured originates from equipment-sized sources with rates larger than 6.0 kg/h. This threshold rate would become even smaller if sources below 3 kg/h were measured at their true density rather than at POD < 1. Emissions monitoring campaigns require both high sensitivity and intensive sampling to accurately capture the emissions distribution.

Acknowledgement

Bridger Photonics thanks the Advanced Research Program Agency – Energy (ARPA-E) MONITOR program and the Montana Board of Research and Commercialization Technology (MBRCT) for supporting the original development of GML hardware and analytics.

Supporting Information Available

The following data files will be available on the journal website at time of publication:

- GML methane emission source detection data at 150 m spatial aggregation (*.csv).
- GML methane emission source detection data at 2 m spatial aggregation (*.csv).
- Single-emitter classification of CM 2019 plume images (*.csv).

- Geospatial polygons bounding GML data set (*.kml).

References

(1) Forster, P.; Storelvmo, T.; Armour, K.; Collins, W.; Dufresne, J.-L.; Frame, D.; Lunt, D. J.; Mauritsen, T.; Palmer, M. D.; Watanabe, M.; Wild, M.; Zhang, H. In *Climate Change 2021: The Physical Science Basis. Contribution of Working Group I to the Sixth Assessment Report of the Intergovernmental Panel on Climate Change*; Masson-Delmotte, V., Zhai, P., Pirani, A., Connors, S. L., Pean, C., Berger, S., Caud, N., Chen, Y., Goldfarb, L., Gomis, M. I., Huang, M., Leitzell, K., Lonnoy, E., Matthews, J. B. R., Maycock, T. K., Waterfield, T., Yelekci, O., Yu, R., Zhao, B., Eds.; Cambridge University Press, 2021; Chapter The Earth's Energy Budget, Climate Feedbacks and Climate Sensitivity, pp 923–1054, see Table 7.15.

(2) Szopa, S.; Naik, V.; Adhikary, P.; Berntsen, T.; Collins, W. D.; Fuzzi, S.; Gallardo, A.; Kiendler-Scharr, Z.; Klimont, H.; Liao, N.; Under, N.; Zanis, P. In *Climate Change 2021: The Physical Science Basis. Contribution of Working Group I to the Sixth Assessment Report of the Intergovernmental Panel on Climate Change*; Masson-Delmotte, V., Zhai, P., Pirani, A., Connors, S. L., Pean, C., Berger, S., Caud, N., Chen, Y., Goldfarb, L., Gomis, M. I., Huang, M., Leitzell, K., Lonnoy, E., Matthews, J. B. R., Maycock, T. K., Waterfield, T., Yelekci, O., Yu, R., Zhao, B., Eds.; Cambridge University Press, 2021; Chapter Short-lived Climate Forcers, pp 817–922, see Fig. 6.16.

(3) Brandt, A. R.; Heath, G. A.; Kort, E. A.; O'Sullivan, F.; Pétron, G.; Jordaan, S. M.; Tans, P.; Wilcox, J.; Gopstein, A. M.; Arent, D.; Wofsy, S.; Brown, N. J.; Bradley, R.; Stucky, G. D.; Eardley, D.; Harriss, R. Methane leaks from North American natural gas systems. *Science* **2014**, *343*, 733–735.

(4) Allen, D. T. Methane emissions from natural gas production and use: Reconciling

bottom-up and top-down measurements. *Current Opinion in Chemical Engineering* **2014**, *5*, 78–83.

(5) Zimmerle, D. J.; Williams, L. L.; Vaughn, T. L.; Quinn, C.; Subramanian, R.; Duggan, G. P.; Willson, B.; Opsomer, J. D.; Marchese, A. J.; Martinez, D. M.; Robinson, A. L. Methane Emissions from the Natural Gas Transmission and Storage System in the United States. *Environmental Science and Technology* **2015**, *49*, 9374–9383.

(6) Marchese, A. J.; Vaughn, T. L.; Zimmerle, D. J.; Martinez, D. M.; Williams, L. L.; Robinson, A. L.; Mitchell, A. L.; Subramanian, R.; Tkacik, D. S.; Roscioli, J. R.; Herndon, S. C. Methane Emissions from United States Natural Gas Gathering and Processing. *Environmental Science and Technology* **2015**, *49*, 10718–10727.

(7) Alvarez, R. A.; Zavala-Araiza, D.; Lyon, D. R.; Allen, D. T.; Barkley, Z. R.; Brandt, A. R.; Davis, K. J.; Herndon, S. C.; Jacob, D. J.; Karion, A.; Kort, E. A.; Lamb, B. K.; Lauvaux, T.; Maasakkers, J. D.; Marchese, A. J.; Omara, M.; Pacala, S. W.; Peischl, J.; Robinson, A. L.; Shepson, P. B.; Sweeney, C.; Townsend-Small, A.; Wofsy, S. C.; Hamburg, S. P. Assessment of methane emissions from the U.S. oil and gas supply chain. *Science* **2018**, *361*, 186–188.

(8) Omara, M.; Zimmerman, N.; Sullivan, M. R.; Li, X.; Ellis, A.; Cesa, R.; Subramanian, R.; Presto, A. A.; Robinson, A. L. Methane Emissions from Natural Gas Production Sites in the United States: Data Synthesis and National Estimate. *Environmental Science and Technology* **2018**, *52*, 12915–12925.

(9) Rutherford, J. S.; Sherwin, E. D.; Ravikumar, A. P.; Heath, G. A.; Englander, J.; Cooley, D.; Lyon, D.; Omara, M.; Langfitt, Q.; Brandt, A. R. Closing the methane gap in US oil and natural gas production emissions inventories. *Nature Communications* **2021**, *12*, 4715.

(10) Duren, R.; Thorpe, A.; McCubbin, I. *The California Methane Survey*; 2020; California Energy Commission. Publication Number: CEC-500-2020-047.

(11) Harriss, R.; Alvarez, R. A.; Lyon, D.; Zavala-Araiza, D.; Nelson, D.; Hamburg, S. P. Using Multi-Scale Measurements to Improve Methane Emission Estimates from Oil and Gas Operations in the Barnett Shale Region, Texas. *Environmental Science and Technology* **2015**, *49*, 7524–7526.

(12) Vaughn, T. L.; Bell, C. S.; Pickering, C. K.; Schwietzke, S.; Heath, G. A.; Pétron, G.; Zimmerle, D. J.; Schnell, R. C.; Nummedal, D. Temporal variability largely explains top-down/bottom-up difference in methane emission estimates from a natural gas production region. *Proceedings of the National Academy of Sciences of the United States of America* **2018**, *115*, 11712–11717.

(13) Johnson, M.; Conrad, B. M.; Tyner, D. R. Creating measurement-based oil and gas sector methane inventories using source-resolved aerial surveys. *Nature Communications Earth & Environment* **2023**, *4*, 139.

(14) Peischl, J.; Eilerman, S. J.; Neuman, J. A.; Aikin, K. C.; de Gouw, J.; Gilman, J. B.; Herndon, S. C.; Nadkarni, R.; Trainer, M.; Warneke, C.; Ryerson, T. B. Quantifying Methane and Ethane Emissions to the Atmosphere From Central and Western U.S. Oil and Natural Gas Production Regions. *Journal of Geophysical Research: Atmospheres* **2018**, *123*, 7725–7740.

(15) Robertson, A. M.; Edie, R.; Field, R. A.; Lyon, D.; McVay, R.; Omara, M.; Zavala-Araiza, D.; Murphy, S. M. New Mexico Permian basin measured well pad methane emissions are a factor of 5-9 times higher than U.S. EPA estimates. *Environmental Science and Technology* **2020**, *54*, 13926–13934.

(16) Popova, O.; Long, G. *Advances in technology led to record new well productiv-*

ity in the Permian Basin in 2021; 2022; U.S. Energy Information Administration, https://www.eia.gov/todayinenergy/detail.php?id=54079.

(17) Schneising, O.; Buchwitz, M.; Reuter, M.; Vanselow, S.; Bovensmann, H.; Burrows, J. P. Remote sensing of methane leakage from natural gas and petroleum systems revisited. *Atmospheric Chemistry and Physics* **2020**, *20*, 9169–9182.

(18) Zhang, Y.; Gautam, R.; Pandey, S.; Omara, M.; Maasakkers, J. D.; Sadavarte, P.; Lyon, D.; Nesser, H.; Sulprizio, M. P.; Varon, D. J.; Zhang, R.; Houweling, S.; Zavala-Araiza, D.; Alvarez, R. A.; Lorente, A.; Hamburg, S. P.; Aben, I.; Jacob, D. J. Quantifying methane emissions from the largest oil-producing basin in the United States from space. *Science Advances* **2020**, *6*, eaaz5120.

(19) Varon, D. J.; Jacob, D. J.; Hmiel, B.; Gautam, R.; Lyon, D. R.; Omara, M.; Sulprizio, M.; Shen, L.; Pendergrass, D.; Nesser, H.; Qu, Z.; Barkley, Z. R.; Miles, N. L.; Richardson, S. J.; Davis, K. J.; Pandey, S.; Lu, X.; Lorente, A.; Borsdorff, T.; Maasakkers, J. D.; Aben, I. Continuous weekly monitoring of methane emissions from the Permian Basin by inversion of TROPOMI satellite observations. preprint at `https://acp.copernicus.org/preprints/acp-2022-749/`.

(20) Sherwin, E.; Rutherford, J.; Zhang, Z.; Chen, Y.; Wetherley, E.; Yakovlev, P.; Berman, E.; Jones, B.; Thorpe, A.; Ayasse, A.; Duren, R.; Brandt, A.; Cusworth, D. Quantifying oil and natural gas system emissions using one million aerial site measurements. preprint at `https://doi.org/10.21203/rs.3.rs-2406848/v1`.

(21) Cusworth, D. H.; Duren, R. M.; Thorpe, A. K.; Olson-Duvall, W.; Heckler, J.; Chapman, J. W.; Eastwood, M. L.; Helmlinger, M. C.; Green, R. O.; Asner, G. P.; Dennison, P. E.; Miller, C. E. Intermittency of Large Methane Emitters in the Permian Basin. *Environmental Science and Technology Letters* **2021**, *8*, 567–573.

(22) Cusworth, D. H.; Thorpe, A. K.; Ayasse, A. K.; Stepp, D.; Heckler, J.; Asner, G. P.;

Miller, C. E.; Yadav, V.; Chapman, J. W.; Eastwood, M. L.; Green, R. O.; Hmiel, B.; Lyon, D. R.; Duren, R. M. Strong methane point sources contribute a disproportionate fraction of total emissions across multiple basins in the United States. *Proceedings of the National Academy of Sciences* **2022**, *119*, e2202338119.

(23) Chen, Y.; Sherwin, E. D.; Berman, E. S. F.; Jones, B. B.; Gordon, M. P.; Wetherley, E. B.; Kort, E. A.; Brandt, A. R. Quantifying regional methane emissions in the New Mexico Permian Basin with a comprehensive aerial survey. *Environmental Science and Technology* **2022**, *56*, 4317–23.

(24) Johnson, M. R.; Tyner, D. R.; Szekeres, A. J. Blinded evaluation of airborne methane source detection using Bridger Photonics LiDAR. *Remote Sensing of Environment* **2021**, *259*, 112418.

(25) Bell, C.; Rutherford, J.; Brandt, A.; Sherwin, E.; Vaughn, T.; Zimmerle, D. Single-blind determination of methane detection limits and quantification accuracy using aircraft-based LiDAR. *Elementa: Science of the Anthropocene* **2022**, *10*, 00080.

(26) National Weather Service, Midland Texas Monthly Wind Averages. [Data set]. https://www.weather.gov/maf/cli_maf_winds (Retrieved 2022-Dec-12).

(27) Thorpe, A.; Frankenberg, C.; Aubrey, A.; Roberts, D.; Nottrott, A.; Rahn, T.; Sauer, J.; Dubey, M.; Costigan, K.; Arata, C.; Steffke, A.; Hills, S.; Haselwimmer, C.; Charlesworth, D.; Funk, C.; Green, R.; Lundeen, S.; Boardman, J.; Eastwood, M.; Sarture, C.; Nolte, S.; Mccubbin, I.; Thompson, D.; McFadden, J. Mapping methane concentrations from a controlled release experiment using the next generation airborne visible/infrared imaging spectrometer (AVIRIS-NG). *Remote Sensing of Environment* **2016**, *179*, 104–115.

(28) Conrad, B. M.; Tyner, D. R.; Johnson, M. R. Robust probabilities of detection and

quantification uncertainty for aerial methane detection: Examples for three airborne technologies. *Remote Sensing of Environment* **2023**, *288*, 113499.

(29) Duren, R. M.; Thorpe, A. K.; Foster, K. T.; Rafiq, T.; Hopkins, F. M.; Yadav, V.; Bue, B. D.; Thompson, D. R.; Conley, S.; Colombi, N. K.; Frankenberg, C.; McCubbin, I. B.; Eastwood, M. L.; Falk, M.; Herner, J. D.; Croes, B. E.; Green, R. O.; Miller, C. E. California's methane super-emitters. *Nature* **2019**, *575*, 180–184.

(30) Thorpe, A. K.; O'Handley, C.; Emmitt, G. D.; DeCola, P. L.; Hopkins, F. M.; Yadav, V.; Guha, A.; Newman, S.; Herner, J. D.; Falk, M.; Duren, R. M. Improved methane emission estimates using AVIRIS-NG and an Airborne Doppler Wind Lidar. *Remote Sensing of Environment* **2021**, *266*, 112681.

(31) Cusworth, D. Methane plumes for NASA/JPL/UArizona/ASU Sep-Nov 2019 Permian campaign. 2021; [Data set]. Zenodo. https://doi.org/10.5281/zenodo.5610307.

(32) Akaike, H. In *Selected Papers of Hirotugu Akaike*; Parzen, E., Tanabe, K., Kitagawa, G., Eds.; Springer New York: New York, NY, 1998; pp 199–213.

Supporting Information

Extension of Methane Emission Rate Distribution for Permian Basin Oil and Gas Production Infrastructure by Aerial LiDAR

William M. Kunkel,* Asa E. Carre-Burritt, Grant S. Aivazian, Nicholas C. Snow, Jacob T. Harris, Tagert S. Mueller, Peter A. Roos, and Michael J. Thorpe*

Bridger Photonics, Inc., 2310 University Way Bldg 4-4, Bozeman, MT 59715, USA

E-mail: William.Kunkel@bridgerphotonics.com; Mike.Thorpe@bridgerphotonics.com

Contents

S1. Spatial aggregation to 150 m sources

Spatial analysis of GML data is performed by first assigning an emission origin point, or "location," to each detected plume. Detections observed at different times are associated with the same location if they are co-located within 2 m. Emission locations were spatially aggregated to 150 m sources by a clustering algorithm that iterates through a list of GML locations to build a temporary table of locations within 150 m to all other locations in the current cluster. After all unclustered locations in the list have been compared to the temporary cluster (sequentially, in fixed arbitrary order), those in the temporary cluster are removed from the waiting list. New clusters are formed in this way until no locations remain in the waiting list.

GML detections can also be aggregated to "facilities" described by polygons enclosing site assets. Facility polygons represent the boundaries around actual groups of surface infrastructure and are usually defined by the facility pad footprint. Polygons can be provided by operators based on site data or generated from aerial photography, in which case the polygon is drawn either manually or by an artificial intelligence model. A mix of AI-generated and manually defined polygons was used in the data set in this work. A polygon is defined for every facility on a GML flight path regardless of whether an emission is actually detected.

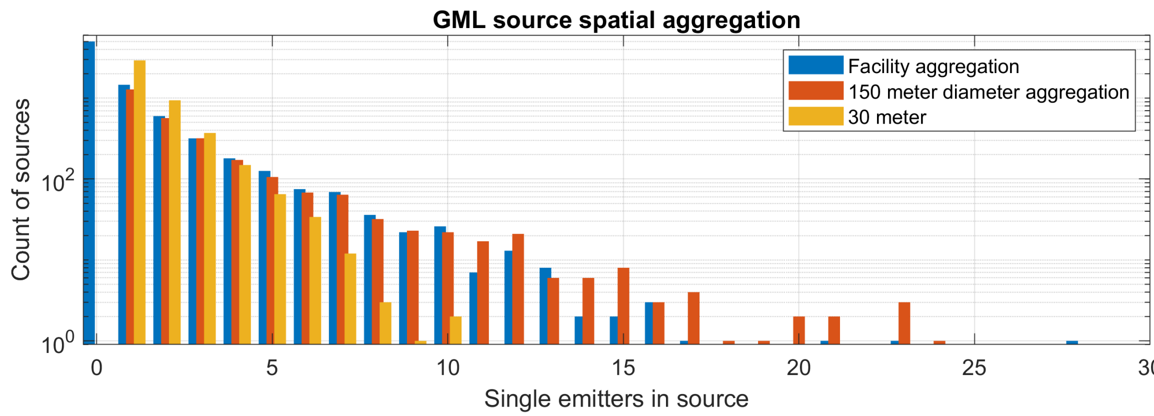

Figure S1: Histogram counting spatially aggregated sources by number of emitters in aggregation area.

Comparing the number of GML locations in each facility to the number per 150 m diameter source shows a near correspondence between the two aggregation styles (Fig. S1), supporting the use of 150 m aggregation to represent facility-sized sources. A smaller aggregation area (30 meters) displays a steeper roll-off in number of detection locations per source. For GML, the proportion of facilities with at least one detection was found to be 38.3% (or 32.9% when considering only first overflights in the 15-minute scan window described in Sect. S2.4.2), much higher than the reported 1.48% rate[S1] of well sites in the CM 2019 campaign. This difference may be explained by differences in detection sensitivity described in the analysis.

S2. Data preparation and alignment

Before jointly analyzing emission detection data from diverse sources, several aspects of data collection and data set composition must be considered. In this section we aim to address some important aspects of data alignment, specifically (1) compilation of GML survey data and types of emitters included, (2) spatial overlap of CM and GML surveys, (3) temporal overlap of CM and GML surveys, and (4) influence of scan repetitions on reported emission rates. In preparation for this work, efforts were made to directly align the data sets as much as possible. Where data sets do not align, limited assumptions of spatial or temporal invariance are used to set up the analysis. These are pointed out where relevant in the details of the data preparation process below.

S2.1 Sample composition and emitter types included

The GML sample is compiled from sets of anonymized survey data collected under contracts for client O&G operators. Survey sets for compilation were chosen for geographical and temporal overlap with CM data without considering analysis results. Whereas CM campaigns blanketed entire geographic areas, GML surveys were targeted to client facilities. Clients were given advance notice of when scans would occur (typ. accuracy ±2-3 days). The sample is comprised of scans of sites belonging to 28 individual operators.

Sites included in the GML sample were in the O&G production sector and do not include midstream/distribution infrastructure. Types of infrastructure included in the GML sample consist of wells, separators, tanks, compressors, flares, vapor recovery units, generators, and facility piping. Equipment types were not identified at every facility scanned, though this capability is currently under development. In this work, CM data have been filtered to exclude detections from O&G pipelines unless otherwise marked. In the CM 2019 data set,[S2] measurements with all *source type* tags were included except for "pipeline" and "NA." For CM 2020-21,[S3] the accepted tags were "tank," "well," "compressor," "processing," and "refinery." Exclusion of pipelines seems to have a negligible effect on the shape of the CM distribution, as shown in Sect. S11.

False positive detections can occur in GML detection data, but practically only near the GML detection limit. For emission rates more than a factor of two above the GML detection limit the likelihood of false positives is vanishingly small. GML uses a physics model of the LiDAR measurement noise processes (shot noise, photodetector noise, speckle noise) to estimate the noise on each methane concentration LiDAR measurement based on received light levels. During processing of GML data the signal to noise ratio for each measurement is used in a statistical algorithm to detect regions of elevated methane concentration. The detected regions of elevated concentration are then submitted to emitter analysis, which only assigns an emission if a hot spot in both detection confidence and concentration is detected at the upwind end of the detected plume.

S2.2 Spatial overlap of CM and GML samples

GML and CM 2019 samples were restricted to the GAO coverage polygons in the Delaware and Midland Basins provided in Ref. S1. Geography is shown in Fig. S2. Restriction to the GAO polygons excludes 29 out of 1756 detected facility sources in CM 2019. GML detection locations occupy a subregion of both GAO polygons. We assume that the complementary area in the GAO polygon does not significantly affect the emission rate distribution.

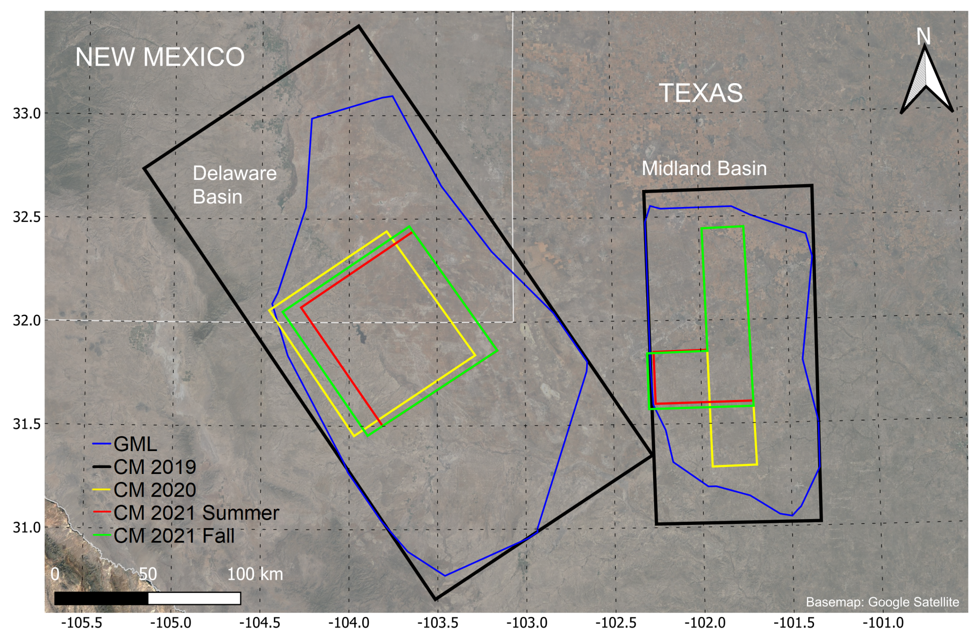

Figure S2: Geospatial domain of GML and CM samples. GML polygons contain all detected emission locations and include a random buffer so vertices do not correspond to detections. CM 2019 polygons reported in Ref. S1 represent areas surveyed at least once by GAO. CM 2020-21 polygons are approximate based on detection coordinates; details reported in Ref. S4.

Though the CM 2020-21 coverage areas[S4] intersect the 2019 GAO polygons, they do not cover the entire area of the 2019 polygons and contain a small amount of additional area outside them. We do not explicitly align GML and CM 2020-21 survey areas in this work, but rather assume that the emission rate distribution is roughly spatially invariant among these areas. We use the same GML data set for joint analysis with CM 2019 and CM 2020-21. We apply no geographic filters to CM 2020-21 other than to select the campaigns that took place in the Permian Basin (*source ID* markers "F," "E," and "J" in the published data set[S3]).

S2.3 Temporal overlap of CM and GML samples

A timeline of plume detections in the GML and CM measurement campaigns is shown in Fig. S3. GML scans were performed between Jan 2020 and Feb 2022, whereas the CM campaigns took place in Sept-Nov 2019 (CM 2019) and Jul 2020-Nov 2021 (CM 2020-21). Analysis in the Results section assumes stationarity in the shape of the emission rate distribution with time (i.e. does not change with choice of time origin). However, stationarity of the scale of the distribution is not required. The joint analysis computes separate likelihoods for each data set and scales the density and cumulative emissions traces to the total density above the CM full detection limit.

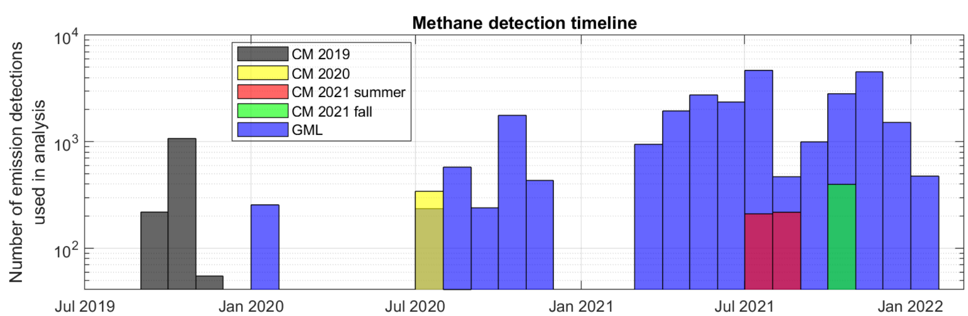

Figure S3: Plume detection counts versus time for CM and GML measurement campaigns.

S2.4 Scan repetitions

CM and GML campaigns were conducted with different approaches to scan repetitions. Number of scans per emission source is shown in Fig. S4. Fewer scans were performed per 150 m source with GML (median: 2 scans) in comparison to CM (2019 median: 6 scans, 2020-21: 4 scans). In CM campaigns, repeated scans over a given source were performed independently of previous results. No minimum number of scans was used to filter the data sets for this work. In GML surveys, repeated scans were performed only on locations where an emission was detected in the first scan. This means that emissions measured by GML were effectively found in just one scan, and repeat measurements were not independent. Most emission sources in the CM campaign had multiple opportunities to be detected, so a greater fraction will have been detected. To address these issues, we describe two solutions below: how to express the distributions in a form that enables direct comparison, and how GML observations are handled considering overflight repetitions and conditionality.

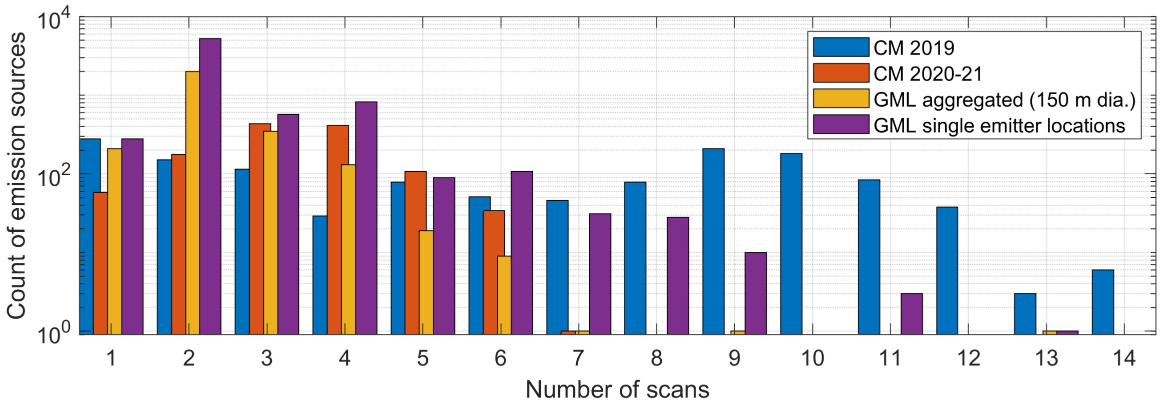

Figure S4: Histogram counting emission sources by number of scan repetitions.

S2.4.1 Transformation to single-scan equivalent

GML and CM distributions are expressed in a "single-scan equivalent" form for alignment. We adopt the notation and terminology of Cusworth et al.[S1] for the persistence-adjusted emission rate $q = f\bar{q}$, where f is the observed persistence $f = M/N$, with M as the number of non-zero unique detections and N as the number of scans, and $\bar{q}$ is the mean of all non-zero measured emission rates

$$\bar{q} = \frac{1}{M}\sum_{i=1}^{M} q_i, \tag{S1}$$

where q_i is a non-zero unique emission rate measurement. For a given source emitting intermittently at a single rate, $\bar{q}$ should be consistent across number of measurement scans, which aids in comparing measurements with different numbers of scans.

To plot emission density and cumulative emission rate on a $\bar{q}$ axis requires further adjustment using the persistence. Consider a point on the detection density function, or rather, a single point in a discrete series representing detection frequency, as shown in Fig. S5a. The persistence adjusted detection frequency (blue), where the emission rate is q, is accessible only from a repetitive sample set and not from a single scan, since the persistence f is needed to obtain q. The detection frequency can be replotted at $\bar{q}$, which effectively removes the persistence from the emission rate. This results in an effectively higher emission rate (green dashed) which overrepresents the density at this emission rate. To obtain a correctly weighted frequency for summation, or density for integration, the prevalence of the source must be reduced by the persistence (red). Where the density or frequency function contains many points, the remapping of q to $\bar{q}$ and the persistence weighting f applies to all points on the curve.

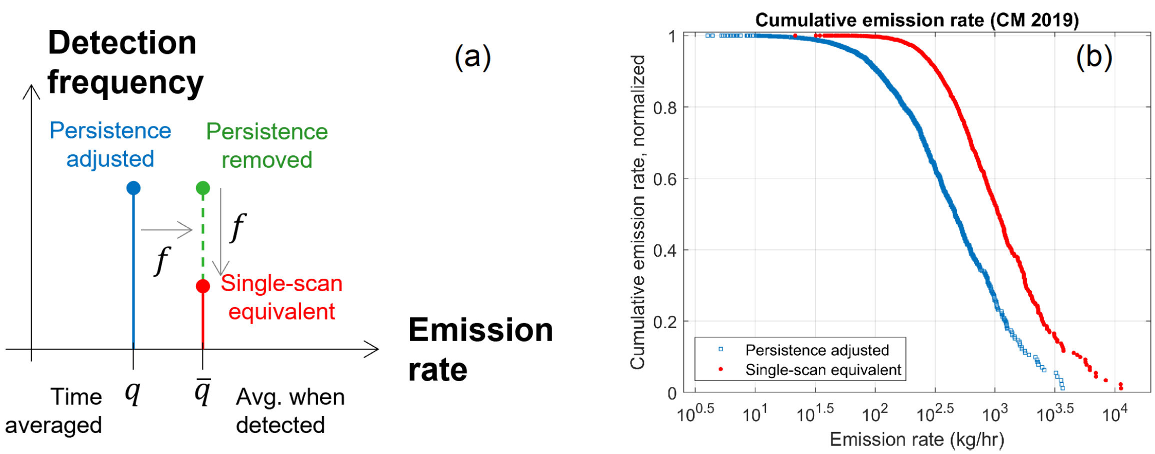

Figure S5: Transformation of emission distribution using the observed persistence f, for (a) a discrete point in a measurement series and (b) the cumulative emission rate distribution (CM 2019, 150 m sources). In both plots, emission rate on the x-axis means either q or $\bar{q}$ as indicated. Distributions shown in (b) follow Eq. S2, reaching the same total emission rate without independent normalization.

Next, consider the implications for the cumulative emission rate distribution. For a finite set of measurements, the cumulative emission rate is computed using the discrete sum

$$c(x) = \frac{1}{\sum q} \cdot \begin{cases} \sum\limits_{q \geq x} q & \text{(persistence adjusted)} \\ \sum\limits_{\bar{q} \geq x} f\bar{q} & \text{(single-scan equivalent)} \end{cases}, \tag{S2}$$

where x is the emission rate. The result of Eq. S2 applied to the CM 2019 sample used for analysis is shown in Fig. S5b. Different forms of the sum yield the same total emission rate since each source contributes the same argument to the sum ($q = f\bar{q}$). Effectively the contributions have been reordered and replotted on the x-axis according to the corresponding value of q or $\bar{q}$. As a result, the single-scan equivalent distribution is a reshaped and horizontally shifted version of the persistence-adjusted distribution.

Although this treatment conveniently transforms distributions for comparison regardless of number of scans, the resulting distributions are not exact. Noting that the observed persistence f is an observation of an event with probability equal to the actual source persistence times the probability of detection (POD), some distortion of the distribution can be expected where sources with POD < 1 from below the FDL are shifted above it. Whereas this affects multi-scan data sets like CM, single-scan data sets (which GML approximates) would not be affected.

S2.4.2 GML detections

GML observations of a given emission source come at three different levels: overflight, location scan, and aggregated source scan. A location scan is comprised of one or more aerial passes ("overflights") of an emission source seen at GML source resolution (~ 2 m). The first measurement out of all overflights within a 15-minute time window, inclusive of measurements with zero and non-zero emission rates, is selected to represent the emission rate for the scan. Scan measurements are then converted to a persistence-adjusted rate q and associated observed persistence f for the location. These are used to find the "average when detected" rate $\bar{q}$ in the same way as for the CM data, using Eq. S1.

For spatially aggregated sources (150 m), emission rates are found by adding the persistence adjusted emission rates for each location in the source, and dividing by a composite persistence value for the source,

$$f_{\text{agg}} = \frac{\sum_i q_{\text{loc},i} f_{\text{loc},i}}{\sum_i q_{\text{loc},i}}, \tag{S3}$$

where $q_{\text{loc},i}$ is the persistence adjusted emission rate and $f_{\text{loc},i}$ is the observed persistence, where both correspond to the i^{th} location in the source. In other words, the aggregated source persistence is an average of the observed location persistence values, weighted by the persistence-adjusted location emission rates. The average emission rate for the source, when detected, is then calculated as $\bar{q} = \sum_i q_{\text{loc},i}/f_{\text{agg}}$.

S3. Statistical test on CM and GML distributions

A two-sample Kolmogorov-Smirnov (K-S) test[S5] is used to check for differences between the tails of the GML and CM samples. This is a non-parametric test with a standard null hypothesis (no statistically significant difference between the samples). Here the test is performed on the survival function for a single-scan equivalent sample,

$$S(x) = \frac{\sum_{\bar{q} \geq x}^{\infty} f(\bar{q})}{\sum_{\bar{q}=x_L}^{\infty} f(\bar{q})}, \tag{S4}$$

where x is the emission rate and $x \geq x_L$, with x_L as the lower bound of a range of interest, and f is the observed persistence for a given measurement with emission rate $\bar{q}$. The sum is represented as a stepwise function for the K-S test. As mentioned in the Results section, we choose $x_L = 600\ \text{kg}\,\text{h}^{-1}$ as the effective full detection limit of CM measurements.

The survival function of the GML and CM 2019 samples are plotted in Fig. S6. The

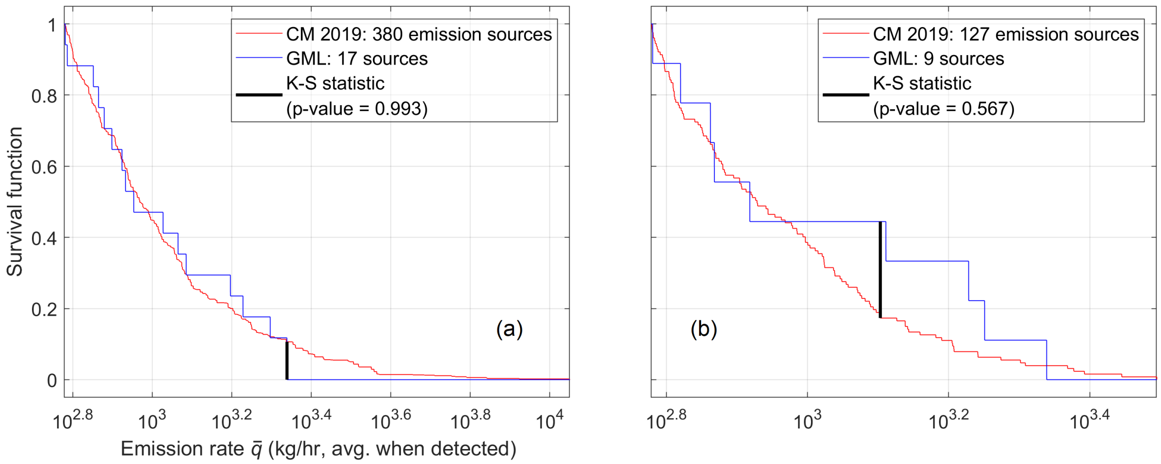

Figure S6: Survival function of single-scan equivalent CM 2019 and GML source detections above 600 $\mathrm{kg\,h^{-1}}$ where sources are defined by a (a) 150 m aggregation diameter and (b) single emitter. Kolmogorov-Smirnov (K-S) statistic and associated p-value are shown.

Kolmogorov-Smirnov (K-S) statistic shows the maximum absolute residual between the two sample distributions. The number of measurements in the GML sample is small in this range. In both cases the associated p-values are high and do not indicate rejection of the null hypothesis.

The K-S test is also used to check the measured emission distribution for the CM 2020-21 campaigns against GML. In 2020-21, CM conducted three campaigns around the Midland and Delaware sub-basins (2020 summer, 2021 summer, 2021 fall). Each campaign is smaller than CM 2019 in number of detections and number of overflights (see Fig. S1). Spatial overlap among these campaigns is partial; overlap with CM 2019 is also partial.[S4] For the analysis in this paper, no controls for spatial overlap were used, under the assumption that the shape of the emission distribution is spatially invariant over the CM 2019 and CM 2020-21 domains. The GML data set is unchanged whether comparing to CM 2019 or CM 2020-21.

Fig. S7 shows the distributions and K-S test results. For the CM 2020 campaign, a deviation around $10^{2.9}$ $\mathrm{kg\,h^{-1}}$ is responsible for a slightly low p-value of 0.166. When grouped with the other campaign data, however, the CM 2020 deviation no longer causes the maximum difference in sample distributions (comparing Fig. S7a and Fig. S7d). For analysis in the rest of this paper, all three CM 2020-21 campaigns were merged into one data set as shown

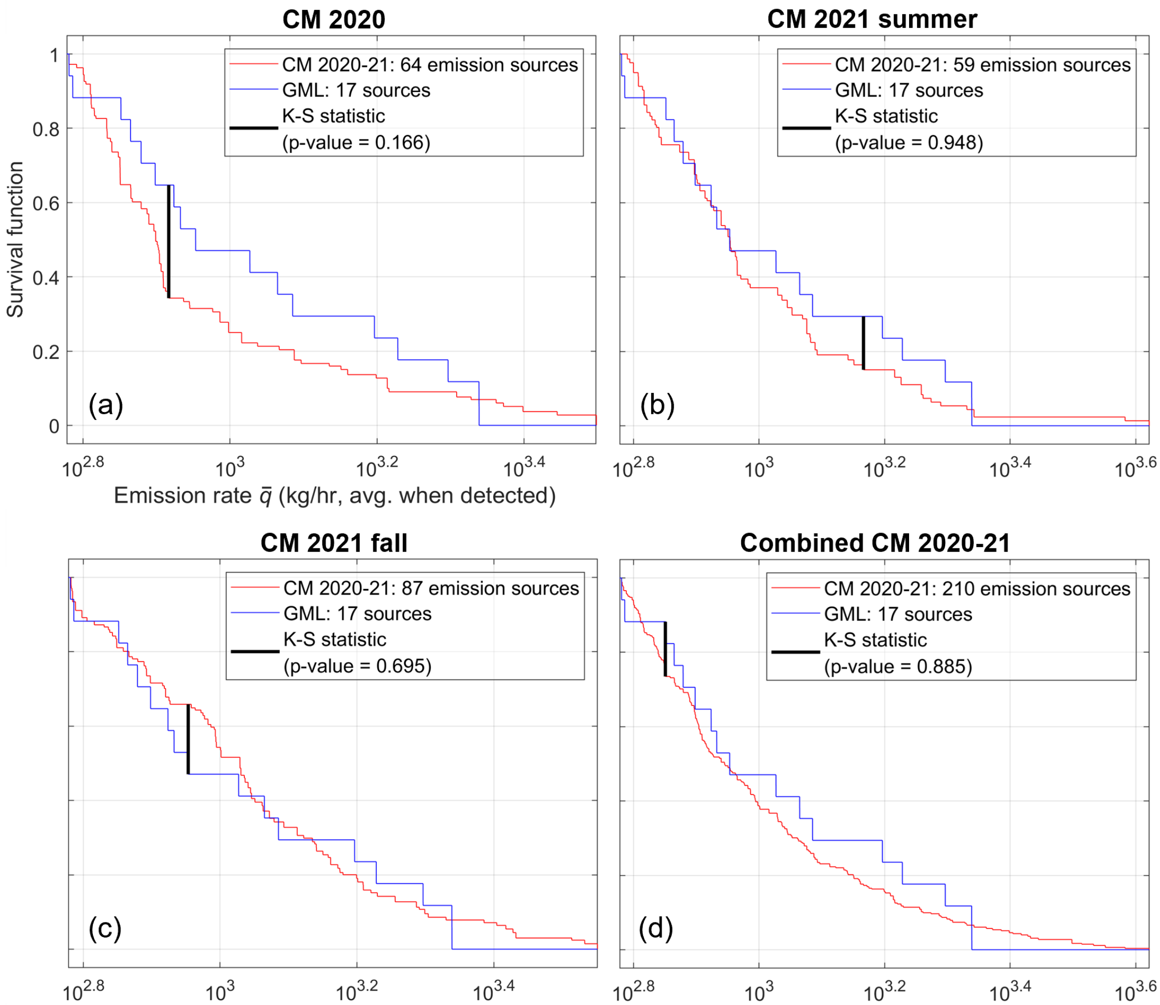

Figure S7: Survival function of CM 2020-21 and GML single-scan equivalent source detections (150 m aggregation diameter) for emission rates above 600 $\mathrm{kg\,h^{-1}}$ for campaigns taking place in (a) 2020 summer, (b) 2021 summer, (c) 2021 fall, and (d) all 2020-21 campaigns together. Kolmogorov-Smirnov (K-S) statistic and associated p-value for each case are indicated.

in Fig. S7d.

S4. Likelihood function

The likelihood function $L(\theta)$, where θ is the vector of fit parameters, is based on the density function from Eq. 1 normalized to the integration range $x_{L,i} \leq x < \infty$,

$$p_i(x) = \frac{m}{bd_i\Gamma(1/m)} \exp\left(-\left|\frac{(x-x_0)}{b}\right|^m\right), \tag{S5}$$

where $x_{L,i}$ is the FDL, $d_i = 1 - \mathrm{sgn}(x_{L,i} - x_0)\Gamma\left[\left|(x_{L,i} - x_0)/b\right|^m, 1/m\right]$, and the subscript i has been added to denote the sample (i.e. GML or CM). Using the standard form for the likelihood function, $L(\theta) = \Pi_{j=1}^n p(X_j|\theta)$, where X_j are the observed emission rates in the sample, we obtain the log likelihood function for the i^{th} sample,

$$LL_i(\theta) = \sum_{j=1}^{n}\left[\ln\left(f_{i,j}/\bar{f}_i\right) + \ln\left(\frac{m}{bd_i\Gamma(1/m)}\right) - \left|\frac{X_{i,j}-x_0}{b}\right|^m\right], \tag{S6}$$

where $\bar{f}_i$ is the mean persistence of the sample in the limited domain $(x \geq x_{L,i})$. The term $f_{i,j}/\bar{f}_i$ performs the persistence weighting (vertical part of the density transformation) from persistence-adjusted to single-scan equivalent described in Sect. S2.4.1 while maintaining the property that $\int_{x_L}^{\infty} p(x)dx = 1$.

For joint fits, because the samples are independent, we take the product of likelihoods to obtain the joint log likelihood function

$$LL(\theta) = \sum_i LL_i(\theta), \tag{S7}$$

where $i = 1, 2$.

S5. Akaike information criterion (AIC) analysis

AIC analysis was performed on lognormal and generalized lognormal fits to single-sample data sets and joint data sets. Results are shown in Table S1. As seen by the location of AIC minima under single-sample fits where the fit is tested with the same sample in the "1" rows, joint fits do not provide the best representation of each single sample. They instead reduce the joint likelihood of the two independent samples taken together, as seen by the location of joint relative AIC minima under joint fit columns in "2" rows. Models fit to the CM distribution alone tend to have very low values of joint relative likelihood of information loss (see "3" rows), suggesting that models fit to the CM samples alone are not predictive of the entire distribution through the range over which GML is assessed ($\geq 3\ \mathrm{kg\,h^{-1}}$ or $\geq 10\ \mathrm{kg\,h^{-1}}$). In addition to the lognormal and generalized lognormal functions shown, log-logistic (with an extra parameter for horizontal shift), Fréchet, Gumbel, and power law model functions were tested but were not optimal in any case.

Table S1: Akaike information criterion (AIC) analysis for different data sets: (a) CM 2019 survey data, 150 m emission sources; (b) CM 2019 survey data, single emitter (or equipment-sized) emission sources; (c) CM 2020-21 survey data, 150 m emission sources. Each table displays (1) AIC values obtained from the likelihood function (parameter values x_0, b, m), (2) relative AIC values $\mathrm{AIC}_{\mathrm{rel},j} = \mathrm{AIC}_{i,j} - \mathrm{AIC}_{\mathrm{min},j}$, where (i, j) signify (sample, fit), and (3) relative joint likelihood of information loss minimization, where the joint likelihood is taken as the product of likelihoods corresponding to each sample, i.e. $\exp[-\sum_j \mathrm{AIC}_{\mathrm{rel},j}/2]$.

(a) CM 2019, 150 m sources

(1)

Fit → ↓ Test	CM Lognorm.	GML Lognorm.	Joint Lognorm.	CM Gen.Logn.	GML Gen.Logn.	Joint Gen.Logn.	Min.
CM	54.0	57.8	55.4	55.9	75.8	57.4	54.0
GML	1873	1080	1081	1112	1081	1083	1080
(Params)	(1.840, 0.880)	(0.880, 1.088)	(0.797, 1.140)	(-4.443, 6.057, 6.224)	(-0.350, 2.167, 3.232)	(0.882, 1.072, 1.929)	

(2)

CM	0	3.8	1.4	1.9	21.9	3.4	
GML	793	0	0.6	32.0	1.4	2.6	
Sum	793	3.8	2.1	33.9	23.3	6.0	2.1

(3)

0	0.41	1	0	0	0.14

(b) CM 2019, single emitter sources

(1)

Fit → ↓ Test	CM Lognorm.	GML Lognorm.	Joint Lognorm.	CM Gen.Logn.	GML Gen.Logn.	Joint Gen.Logn.	Min.
CM	-166	-164	-164	-164	-154	-158	-166
GML	67852	3499	3499	6414	3484	3486	3484
(Params)	(2.346, 0.541)	(0.303, 1.056)	(0.311, 1.052)	(-6.901, 9.355, 16.52)	(0.654, 0.731, 1.531)	(0.629, 0.770, 1.619)	

(2)

CM	0	1.8	1.7	1.4	12.1	7.8	
GML	64336	14.1	14.2	2930	0	1.8	
Sum	64336	15.9	15.9	2931	12.1	9.7	9.7

(3)

0	0.04	0.04	0	0.30	1

(c) CM 2020-21, 150 m sources

(1)

Fit → ↓ Test	CM Lognorm.	GML Lognorm.	Joint Lognorm.	CM Gen.Logn.	GML Gen.Logn.	Joint Gen.Logn.	Min.
CM	-137	-129	-136	-136	-129	-130	-136
GML	14235	1080	1081	1625	1082	1082	1080
(Params)	(2.650, 0.500)	(0.880, 1.088)	(0.928, 1.059)	(-4.713, 7.623, 17.04)	(-0.350, 2.167, 3.232)	(-1.957, 3.599, 4.494)	

(2)

CM	0	7.8	7.1	1.0	7.8	6.9	
GML	13155	0	0.2	544	1.4	1.9	
Sum	13155	7.8	7.4	545	9.2	8.7	7.4

(3)

0	0.81	1	0	0.39	0.50

S6. Model fit and scaling

Results from the fit optimization for CM 2019 (150 m sources) are shown in Fig. S8. Measured data in each survival function are plotted according to Eqn. S4, which scales each sample to $S(x_{L,i}) = 1$ at the respective FDL, $x_{L,i}$, where i denotes the sample. The model function is correspondingly normalized using integrals over the density $p_i(x)$ given by Eqn. S5.

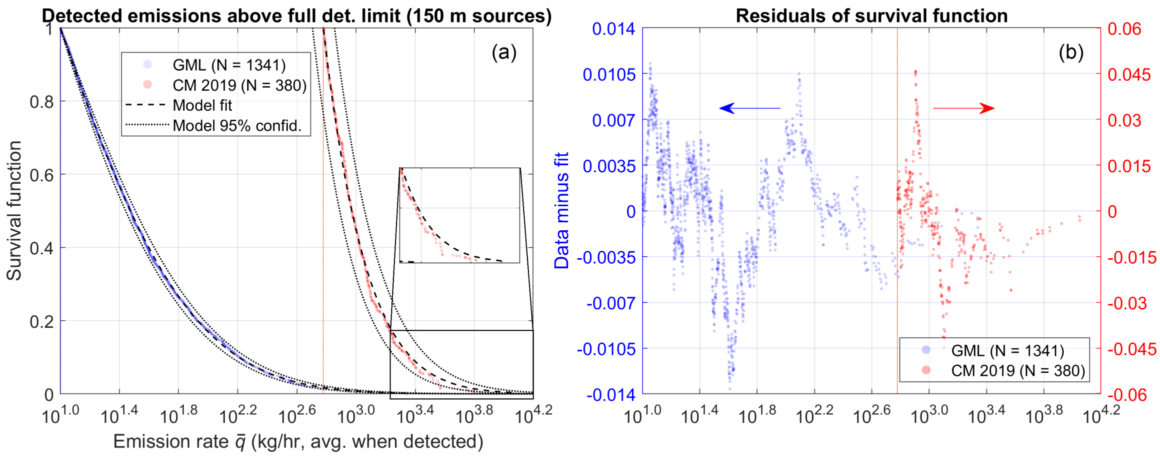

Figure S8: Joint model fitting of 150 m aggregated emission sources showing (a) survival function and (b) fit residuals. Inset: zoomed-in view of largest CM emission rates.

Residuals for both traces show that the survival function crosses the model multiple times without a strong bias toward the positive or negative values. However, CM residuals are negative for emission rates above roughly $10^{3.4}$ kg h^{-1}. This does not strongly impact the density function fit, but it does influence sample agreement with the model for cumulative emissions (i.e. the integral of the density function weighted by emission rate).

When plotted as density functions as in Fig. 2, traces are scaled to a common reference. The factor $1000/n_{\mathrm{CM}}(x > x_{L,\mathrm{CM}})$ is used to scale the CM data to 1000 detections above the CM FDL, where n is the number of detected sources in the specified range. The GML series is scaled by the factor

$$\frac{1000}{n_{\mathrm{GML}}(x > x_{L,\mathrm{GML}})} \frac{1}{\int_{x_{L,\mathrm{CM}}}^{\infty} p_{\mathrm{GML}}(x)}, \tag{S8}$$

where "CM" or "GML" fill in the subscript i in Eqn. S5. The right-hand term of Eqn. S8 rescales the number of detected sources above the GML FDL by the ratio of the survival functions to each FDL, where both terms in the ratio are evaluated at the CM FDL (that is, recognizing the numerator as $1 = \int_{x_{L,\mathrm{CM}}}^{\infty} p_{\mathrm{CM}}(x)$). These scale factors assume that the size of both samples is sufficiently large above the respective FDL and that sample error in the number of detected sources is negligible. Likewise, the model function is scaled by the factor $1000/\int_{x_{L,\mathrm{CM}}}^{\infty} p_{\mathrm{GML}}(x)$ but with no assumptions about sample size.

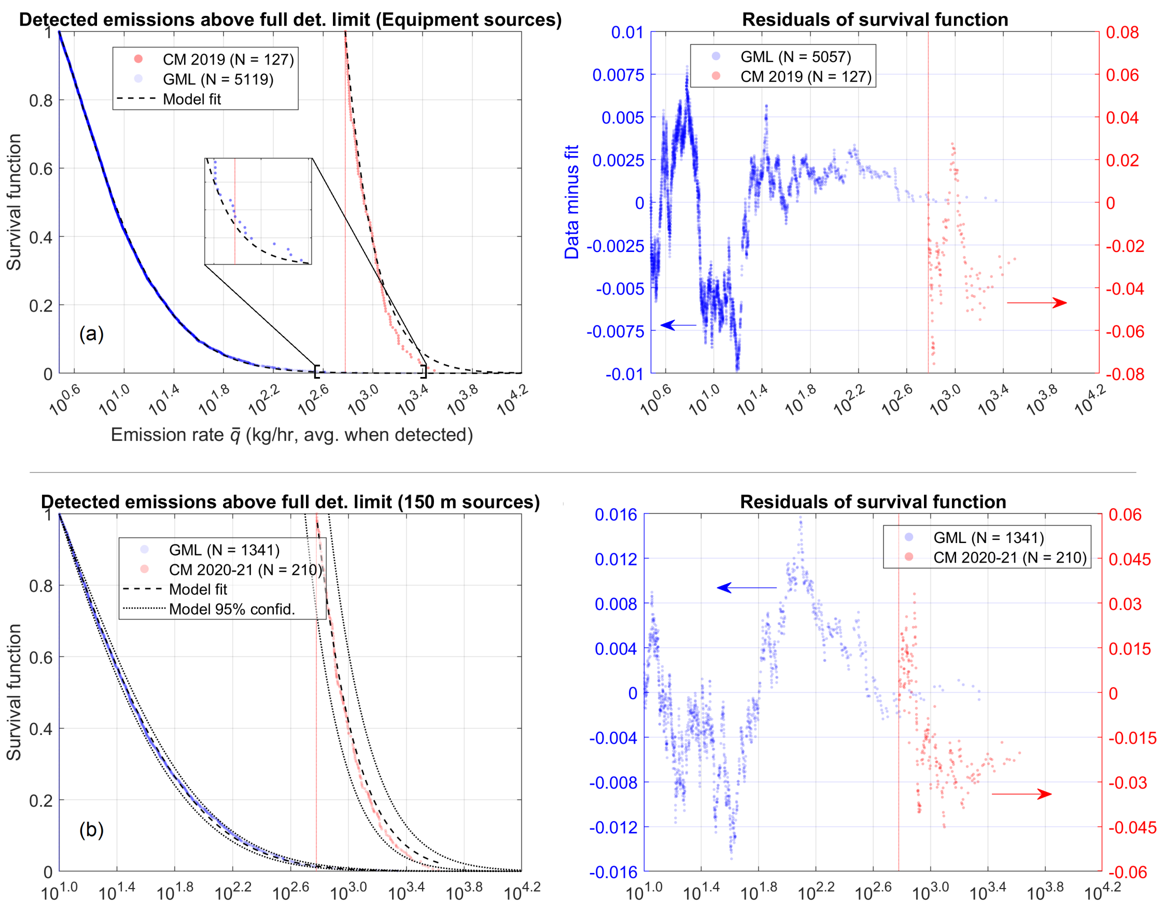

Figure S9: Survival function and residuals showing joint model fitting of GML to (a) CM 2019 equipment-scale sources and (b) CM 2020-21 facility-scale sources (150 m diameter). Inset (a): zoomed-in view of largest GML emission rates.

Fit results in terms of the survival function are shown for CM 2019 equipment-scale sources and CM 2020-21 150 m sources in Fig. S9. In cases where the CM residuals tend to be negative but GML residuals tend to be positive, the fit is located in between the two samples. To some extent, the model disagrees with CM due to the GML measurements in these cases. Other possible reasons for the fit to be above the CM measurement distribution in the heavy tail include (1) the model functional form or parameter values do not adequately represent the rapid decline in sources in the heavy tail, or (2) the heavy tails measured by CM are reshaped relative to GML by other factors such as quantification bias, such as that reported in Ref. S6. Assuming that the CM and GML measured distributions are in fact aligned, apparent differences may be explained by the heavy tail of the distribution rolling off faster than the model fits above emission rates of roughly $10^{3.4}$ $\mathrm{kg\,h^{-1}}$.

S7. Equipment-scale emission source filtering

Human analysts classified CM 2019 plume images in a binary fashion as either "single emitter" or "multiple or unclear." Detections classified as "single emitter" were selected for analysis. Scan data were cut to include only the first scan at each source, making the data set effectively single-scan ($f = 1$). This filter changed the number of CM 2019 sources after other filters (removing pipelines, restricting to GAO survey polygons) from 1348 at 150 m to 645 single emitters. For GML, skipping aggregation increased the number of GML sources from 2727 to 7176, though the number of GML sources above the CM FDL shrank from 17 to 9. Spatial aggregation significantly affects the CM distribution, whereas O&G pipeline sources do not (Section S11). Fit residuals display similar behavior to those from 150 m sources (Sect. S6).

S8. Density plots (CM 2019 single emitters, CM 2020-21)

Detected emission density from analysis with CM 2019 single emitter and CM 2020-21 samples is shown in Fig. S10. As shown in Fig. S10a, the CM 2019 single emitter sensitivity at 50% POD is seen to be 321 [277, 382] $\mathrm{kg\,h^{-1}}$. This overlaps with the confidence interval of the CM 2019 detection sensitivity at 150 m aggregation. Further details of the single emitter distribution in contrast to the 150 m distribution are described around Fig. 3. For the CM 2020-21 sample, Fig. S10b shows the density with CM 2019 traces reproduced for comparison. The sensitivity at 50% POD is 252 [227, 282] $\mathrm{kg\,h^{-1}}$, which suggests a possible improvement over the CM 2019 campaign sensitivity (possibly from flight altitude; CM 2020-21 campaigns were flown at 4.5 km AGL only). The CM 2020-21 sample is scaled to the CM 2019 sample using the ratio of the GML scale values given in Eqn. S8 from analysis with both CM samples, a value of 0.833. This ensures that the CM traces are scaled to one another such that the GML traces from both analyses coincide exactly. In other words, the CM traces are both scaled to 1000 total CM 2019 detections above the CM FDL using the GML distribution as a common reference.

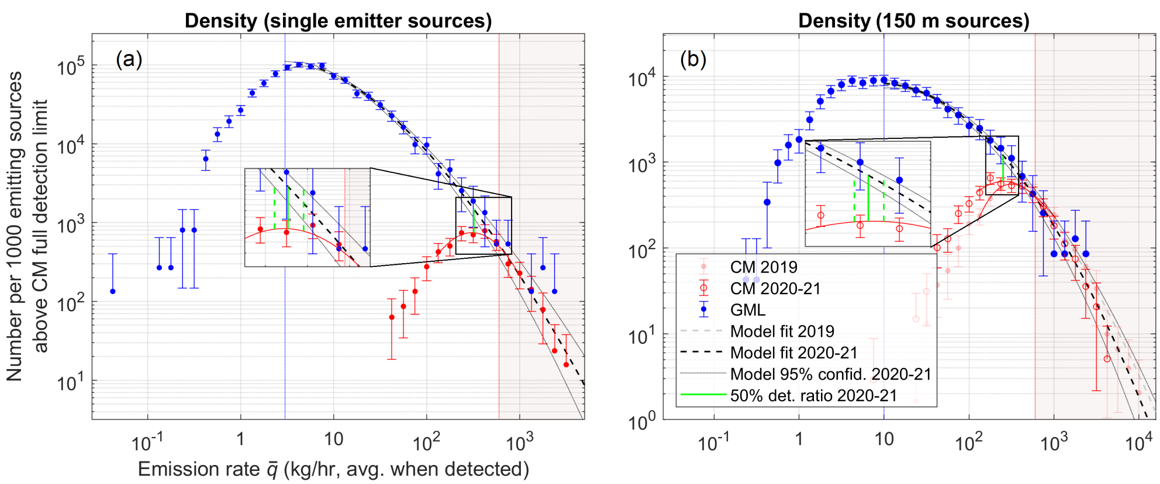

Figure S10: Emission source density from joint analysis with GML for (a) CM 2019 single emitters and (b) CM 2020-21 with 150 m sources. Zoomed in view near the CM sensitivity (insets) shows the 50% detection ratio with respect to model function, along with confidence bounds (dashed green). Model function for CM 2020-21 (150 m) distribution follows Eq. 1 with $m = 2$, $x_0 = 0.928$, $b = 1.059$.

S9. Cumulative emission rate distribution (CM 2020-21)

The CM 2020-21 cumulative emission rate distribution is displayed in Fig. S11. CM 2019 measured data and model function are reproduced in the plot for comparison. Both CM data sets were analyzed jointly with the GML data set. By comparing the measured distributions at 10 $\mathrm{kg\,h^{-1}}$ to the model function and its confidence bounds at this emission rate, we find that CM 2020-21 measured 43.4% [37.8%, 49.2%] of the total cumulative emission rate from 150 m sources above 10 $\mathrm{kg\,h^{-1}}$, whereas GML measured 98.2% [85.5%, 111.3%]. These results are similar to those obtained with CM 2019 data, suggesting consistency between the CM 2019 and 2020-21 campaigns.

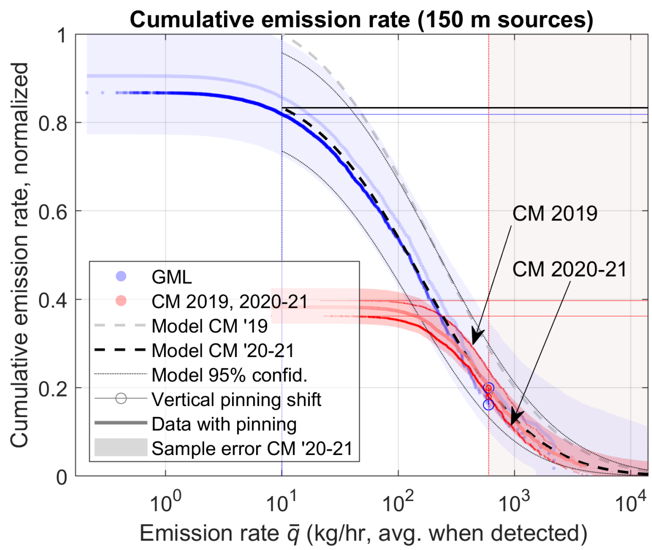

Figure S11: Cumulative emission rate distribution of GML and CM 2020-21 measurements with 150 m diameter aggregated emission sources. Joint GML/CM 2019 model and CM 2019 measured distribution are reproduced for comparison. Distributions from CM 2020-21 joint analysis are scaled to those from the CM 2019 analysis. All traces are normalized to equivalent campaign scale (spatial area, number of overflights). Vertically shifted copies of measured data pinned to the value of the model distribution at the CM FDL guide the eye to suggest the shape of the measured distribution supposing sample error above the CM FDL were suppressed.

Relative scaling of the CM 2020-21 density function to CM 2019 results in the different cumulative emission rate totals shown in the plot. This was performed as described in Sect. S8, where GML density was used as a reference. GML to CM scaling is implied directly from the joint fit without any ad hoc parameters. The ratio of measured totals between the two campaigns (CM 2020-21/CM 2019) is 91% when scaled to one another accounting for sample size and number of overflights, using GML as a reference.

S10. Monte Carlo estimation of sample error

A Monte Carlo algorithm is used to obtain percentile ranges on the cumulative emission rate as a function of source emission rate. New samples are synthesized from the joint best-fit density function at emission rates above the respective FDL. Size of synthesized samples matches the number of detected sources above the FDL in the measured samples. Since the density function expresses the single-scan equivalent, the number of overflights is one for each synthesized detection. For each of n_{MC} =10,000 Monte Carlo trials, a vector of $n(x < x_{L,i})$ random numbers uniformly distributed on the interval $(0, 1)$ is generated. The random numbers are input as arguments to the inverse of the survival function on the domain above the FDL to generate source emission rates. Cumulative emission rate versus source emission rate is calculated from each Monte Carlo trial. Percentiles are found from the set of synthesized Monte Carlo trials on a grid of source emission rates.

Simulated sample error supports the emission rate domain down to each respective FDL. Sample error below the FDL is represented by assuming the same cumulative emission rate increase as the measured sample, with no additional error contributed by samples below the FDL.

S11. Exclusion of pipelines from CM data set

Exclusion of O&G pipeline sources in the CM 2019 sample produces negligible change in the survival function. By comparison, the effect of filtering the data to single emitter sources changes the distribution significantly. Fig. S12 shows the survival function for "with pipeline" and "without pipeline" filters for 150 m and single emitter aggregation styles. Moderate p-values, and hence no statistically significant difference, are seen between the distributions including or excluding pipelines within each aggregation style. However, the p-value for a comparison across aggregation styles is outside the 95% confidence interval ($p < 0.05$), indicating that those distributions differ significantly.

Despite the lack of significant change in the shape of the CM 2019 distribution with the inclusion or exclusion of pipelines, small differences around the detection roll-off ($300\ \mathrm{kg\,h^{-1}}$) lead to slightly different estimates of the detection sensitivity. Density functions for both aggregation styles with and without pipelines are shown in Fig. S13. Comparing the model bounds at 95% confidence to respective cubic polynomial roll-off fits yields detection sensitivity intervals of 233-279 (with pipelines) and 256-309 $\mathrm{kg\,h^{-1}}$ (no pipelines) for 150 m sources, and 258-356 and 277-382 $\mathrm{kg\,h^{-1}}$, respectively, for single emitter sources. Since these intervals overlap significantly, the detection sensitivity roll-off can be considered as weakly dependent on both types of data filter.

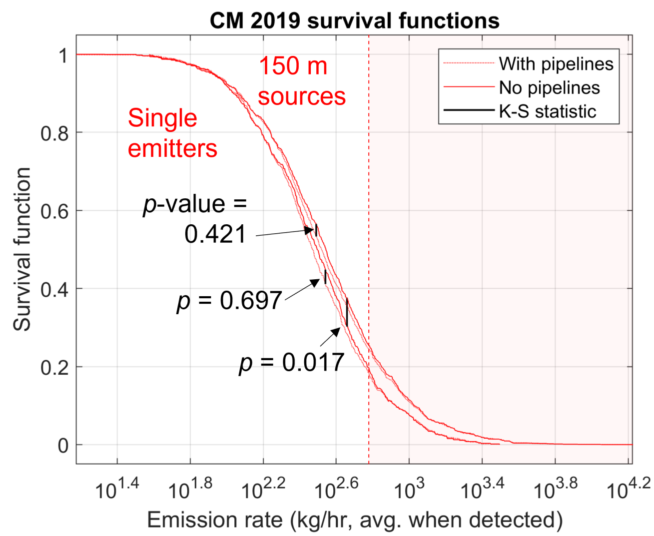

Figure S12: Comparison of CM 2019 survival functions over the range of emission rates in the sample. Data are filtered to either include or exclude O&G pipeline emission sources at both 150 m aggregation and single emitter sources. p-values are indicated for "with pipeline" and "without pipeline" comparisons within each source type and a "no pipeline" comparison across the two source types.

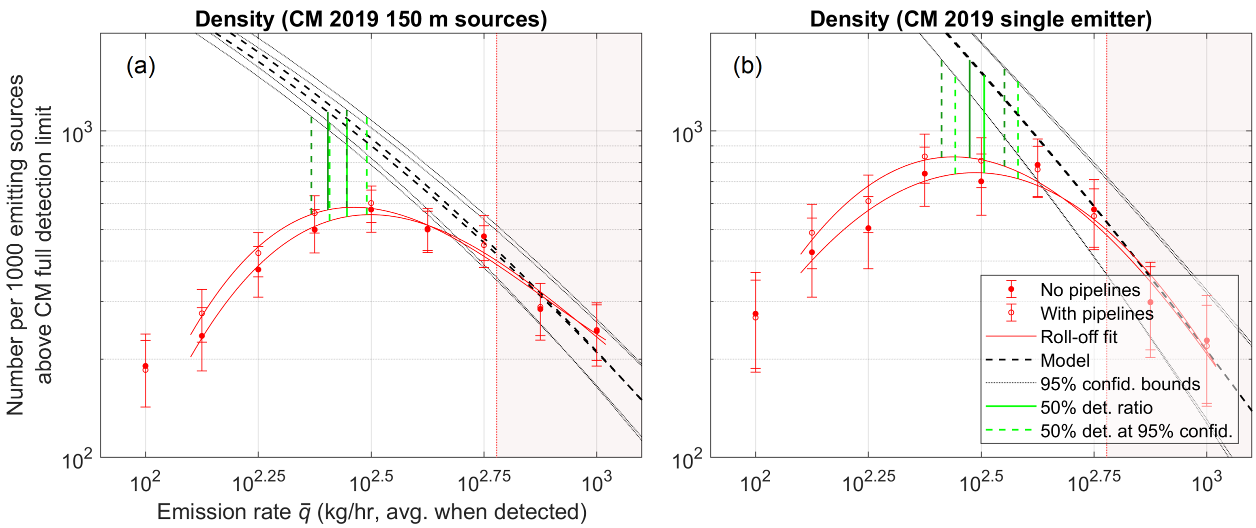

Figure S13: CM 2019 detected emission density plots showing influence of O&G pipeline sources on emission distribution around detection roll-off for 150 m aggregated sources (a) and single emitter sources (b). Model functions are reproduced from joint analysis with GML.

References

[S1] Cusworth, D. H.; Duren, R. M.; Thorpe, A. K.; Olson-Duvall, W.; Heckler, J.; Chapman, J. W.; Eastwood, M. L.; Helmlinger, M. C.; Green, R. O.; Asner, G. P.; Dennison, P. E.; Miller, C. E. Intermittency of Large Methane Emitters in the Permian Basin. *Environmental Science and Technology Letters* **2021**, *8*, 567–573.

[S2] Cusworth, D. Methane plumes for NASA/JPL/UArizona/ASU Sep-Nov 2019 Permian campaign. 2021; [Data set]. Zenodo. https://doi.org/10.5281/zenodo.5610307.

[S3] Cusworth, D. Methane plumes from airborne surveys. 2021; [Data set]. Zenodo. https://zenodo.org/record/7072824#.ZELKvM7MKUm.

[S4] Cusworth, D. H.; Thorpe, A. K.; Ayasse, A. K.; Stepp, D.; Heckler, J.; Asner, G. P.; Miller, C. E.; Yadav, V.; Chapman, J. W.; Eastwood, M. L.; Green, R. O.; Hmiel, B.; Lyon, D. R.; Duren, R. M. Strong methane point sources contribute a disproportionate fraction of total emissions across multiple basins in the United States. *Proceedings of the National Academy of Sciences* **2022**, *119*, e2202338119.

[S5] Bartoszyński, R.; Niewiadomska-Bugaj, M. *Probability and Statistical Inference*; Wiley, 1996; Chapter 16.

[S6] Rutherford, J. S.; Sherwin, E. D.; Chen, Y.; Aminfard, S.; Brandt, A. R. Evaluating methane emission quantification performance and uncertainty of aerial technologies via high-volume single-blind controlled releases. preprint at https://doi.org/10.31223/X5KQ0X.